PHYSICAL REVIEW LETTERS **129,** 147801 (2022)

Biopolymer Filament Entanglement Softens Then Hardens with Shear

Kaikai Zheng,[1,*] Zitong Zhang,[2,*] Bingyang Cao,[2] and Steve Granick[1,3,†]
[1]*Center for Soft and Living Matter, Institute for Basic Science (IBS), Ulsan 44919, Korea*
[2]*School of Aerospace, Tsinghua University, Beijing 100084, People's Republic of China*
[3]*Departments of Chemistry and Physics, Ulsan National Institute of Science and Technology (UNIST), Ulsan 44919, Korea*

(Received 16 May 2022; accepted 23 August 2022; published 28 September 2022)

It is unsatisfactory that regarding the problem of entangled macromolecules driven out of equilibrium, experimentally based understanding is usually inferred from the ensemble average of polydisperse samples. Here, confronting with single-molecule imaging this common but poorly understood situation, over a wide range of shear rate we use single-molecule fluorescence imaging to track alignment and stretching of entangled aqueous filamentous actin filaments in a homebuilt rheo-microscope. With increasing shear rate, tube "softening" is followed by "hardening." Physically, this means that dynamical localization first weakens from molecular alignment, then strengthens from filament stretching, even for semiflexible biopolymers shorter than their persistence length.

DOI: 10.1103/PhysRevLett.129.147801

The entanglement of long, threadlike polymers, a fundamental concept in polymer physics, is believed to be at the core of ubiquitous natural phenomena from the processing of plastics to transport in the cell cytoskeleton. Its dynamical consequences have been modeled with increasing sophistication as "reptation" along a coarse-grained snakelike "tube" [1–5], but these concepts were developed to describe Brownian diffusion at equilibrium. Too little is known from spatially addressed measurements about tubes in out-of-equilibrium situations. Here, we are concerned primarily with the problem of chains whose length is intermediate: too long to be considered as rigid rods, too short to be considered flexible.

While it is true that voluminous literature documents and analyzes the nonlinear rheological and scattering responses of various macromolecules out of equilibrium, measurements of this kind are ensemble averaged and do not discriminate among subpopulations of different molecules. Important single-molecule experiments involving active and passive microrheology have been reported [6–9], but by design, such experiments did not impose shear fields on the entire sample. The computer simulation literature is limited regarding the accessible spatiotemporal scales [3–5]. From the experimental point of view, the absence of single-molecule resolution in parallel with concomitant macroscopic measurements has been a bottleneck.

Early theory predicted that because stretched chains rapidly retract within a sheared or stretched tube, macroscopic deformations do not modify the tube diameter [10,11]. Subsequently, tube expansion was predicted owing to deformation-induced chain orientation [2,12], while other theory predicted tube compression when chains are stretched affinely [13,14], and still other theory predicts nonmonotonic dependence on strain and strain rate [15]. Upon surveying the vast theoretical literature regarding tube theories of threadlike molecules, it is interesting to observe that the bulk of it has gone toward understanding dynamic localization at rest, with less deep theoretical scrutiny of nonlinear behavior. To the best of our knowledge, no current experimental evidence resolves these issues.

Here, we select for study a system of semiflexible biopolymer filaments that displays extremely strong sensitivity to imposed shear. It was shear thinning even at the lowest shear rates accessible to us; stated equivalently, stress increased with increasing shear rate and appeared to saturate at a limiting shear stress that may reflect signifying wall slip [16] (Supplemental Material, Fig. 1 [17]). The power-law decay of approximately −0.6 is close to a theoretical prediction 0.64 for weakly entangled polymers [18]. Filamentous actin (F-actin) networks were selected since these filaments are long enough to be visualized individually, *in situ* during shear, by epifluorescence microscopy. The mean filament length of 10 μm (number averaged) has, from the sample preparation, weight-average to number-average polydispersity of 1.3 and persistence length 17 μm [19]. In a homebuilt modification of a commercial rheometer (Anton Par Model MCR 502, Anton Par) equipped with an air bearing and a cone-plate measuring system with diameter 4 cm and cone angle 1° [20], we performed epifluorescence imaging of individual molecules during macroscopically imposed shear based on the optical setup drawn in Fig. 2 of Supplemental Material [17]. Using a 100× oil objective (actin labeled with Alexa 568 dye at labeling ratio 1:1000), and observation plane deep within the sample ($\approx$100 μm) to avoid potential wall effects, the selected F-actin concentration of 1 mg/mL is the highest concentration that avoids entering the nematic

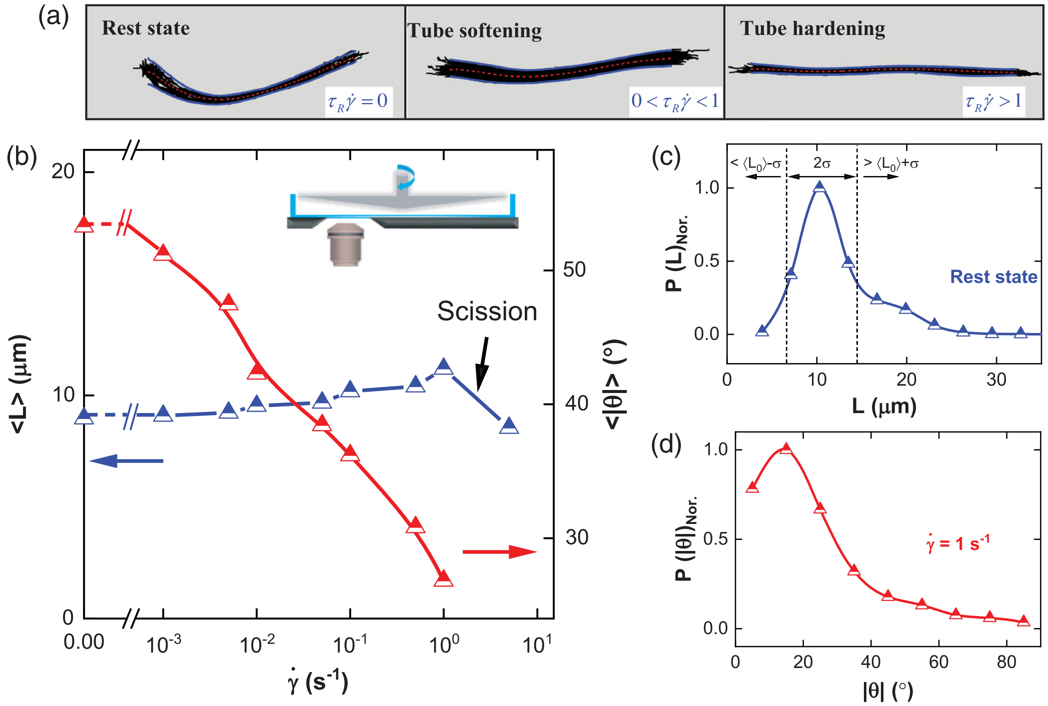

FIG. 1. *In situ* single-molecule imaging of entangled F-actin under shear. (a) "Tube" trajectories, each of a different single filament, after removing the mass center velocity, compared in the rest state, in the tube-softening regime (shear rate 0.1 s^{-1}) and in the tube-hardening regime (shear rate 1 s^{-1}). (b) As a function of logarithmic shear rate, this graph shows the mean filament length $\langle L\rangle$ and the orientation angle $\langle|\theta|\rangle$ with respect to shear, where $\langle\rangle$ denotes the ensemble average of chains with different L. (c) The distribution of L in the rest state, showing standard deviation σ, normalized to the peak value. (d) The distribution of $|\theta|$ at shear rate 1 s^{-1}, normalized to the peak value.

phase during shear [21–23]. It offers degree of entanglement $N/N_e \approx 14$ (N is the degree of polymerization and N_e the entanglement onset). For this degree of entanglement, the reptation time is believed to be $\tau_{\rm rep} \approx 10^3$ s (17 min) [24,25]. Therefore we equilibrated each sheared state for 20 min as we increased the shear rate from 0.001 to 5 s^{-1} in eight steps, and waited 30 min between successive shear rates.

The experimental setup allowed us, *in situ* during shear, to image the effective tube that represents the collective topological influence of surrounding chains. Such measurements exist in the literature regarding actin filaments in the rest state [19,26,27], but we are unaware of prior reports of measurements during shear. Anticipating findings quantified later in this Letter, Fig. 1(a) shows images of the tube profile that we imaged at rest, at modest shear rate, and at high shear rate. In Fig. 1(b), the mean value of filament length L, projected in the focal plane, is seen to increase gently with shear rate $\dot{\gamma}$, presumably from a combination of chain stretch and progressively larger alignment in the focal plane [28–30]. Shear-induced filament scission causes L to decrease abruptly when the shear rate exceeds 1 s^{-1}; therefore, the analysis is restricted to lesser shear rates at which filaments remain intact. Figure 1(b) also plots against shear rate the mean angle θ of filaments in the shear direction, which decreases monotonically with increasing shear rate, indicating progressively greater alignment in the shear direction. However, given the polydispersity, the underlying distributions of normalized L [Fig. 1(c)] and normalized θ [Fig. 1(e)] are so broad that it is fair to question how meaningful these mean values are.

The polydisperse population was binned into three groups: those chains whose L is within a standard deviation of the mean, those chains that are even shorter, and those chains that are even longer. In the absence of shear, the mean is $\langle L_0\rangle \approx 10\ \mu$m and $\sigma \approx 3\ \mu$m is the standard deviation. Considering the entanglement degree z, which is proportional to L, $z = L/l_e = L/\xi^{4/5} l_p^{1/5}$ [31], where l_e, ξ, and l_p are the entanglement length, mesh size, and persistence length, respectively. Because the Rouse relaxation time cannot at this time be determined directly from experiment (to do so would require measuring stress relaxation after sudden strain, but actin filaments are prone to chain scission when stretched rapidly), we estimate the Rouse relaxation time as $\tau_R = \tau_e Z^2$, where τ_e is the calculated entanglement time $\tau_e \sim \xi^{16/5} l_p^{-1/5} \approx 0.23$ s [31]. In this way, for the short, medium, and long chains we estimate Rouse relaxation times 19, 37, and 96 s, respectively. We used the average (45 s) to estimate the Rouse-Weissenberg number $\tau_R\dot{\gamma}$ plotted as the abscissa of

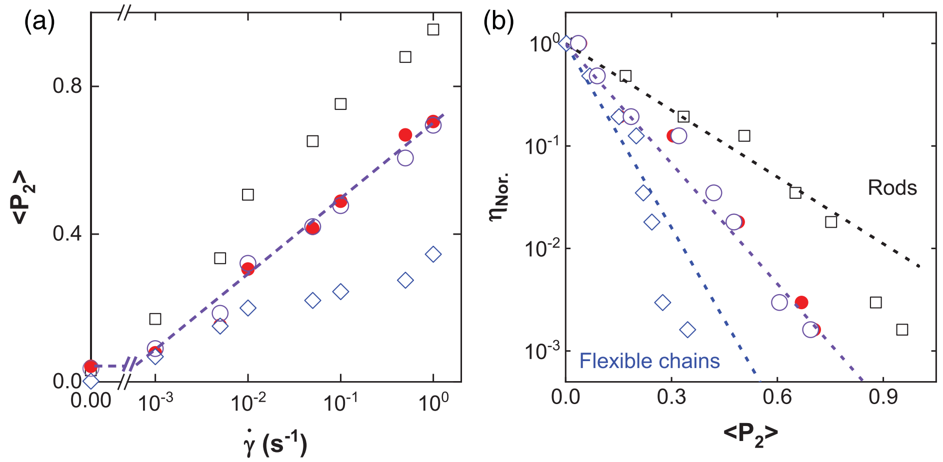

FIG. 2. Correlation between filament alignment and shear thinning. (a) Plotted against logarithmic shear rate, the orientation parameter of F-actin filaments shows strongest dependence for the subpopulation of shortest filaments (squares) and weakest dependence for the subpopulation of longest filaments (diamonds). The middle population (filled circles) and the mean of all populations (open circles) are indistinguishable and indicated by the dotted line. (b) Logarithmic viscosity, normalized to the value measured at 0.001 s^{-1}, is plotted against mean orientation parameter $\langle P_2 \rangle$ and compared to experimental data for rigid rods [33] and flexible chains [32] as indicated.

Fig. 1 of Supplemental Material [17]. Next, from the orientation angle (θ) we extract the orientation parameter (P_2) of the three subpopulations of different L using the relation $P_2 = 1.5\cos^2(\theta) - 0.5$ [32]. Plotted in Fig. 2(a), this quantity increases monotonically with increasing logarithmic shear rate, indicating progressively more alignment. Interestingly, shorter chains display the strongest dependence on shear rate, as predicted theoretically to reflect their lesser flexibility [2].

The trends are consistent when we compare the dependence on shear rate in Fig. 2(a) to that for viscosity (Supplemental Material, Fig. 1 [17]). In the former, the ensemble-averaged $\langle P_2 \rangle \sim 0.2 \log(\dot{\gamma})$ implies $\dot{\gamma} \sim 10^{5\langle P_2 \rangle}$. Combined with the measured dependence of viscosity on shear rate (Supplemental Material, Fig. 1), one predicts shear thinning according to $\eta/\eta_0 \sim \exp(-9.8\langle P_2 \rangle)$, which is not far from the measured prefactor of 9.

It is interesting to compare to other systems, though the available data are ensemble averaged. For a concentrated solution of a rigid rodlike virus, whose contour length is much less than its persistence length ($L/L_p \sim 0.3$), the logarithmic viscosity also shear thins exponentially with $\langle P_2 \rangle$ and the prefactor is 5 [33]. For flexible wormlike micelles, whose contour length much exceeds the persistence length ($L/L_p \sim 10$), this relation also decays exponentially but with prefactor 14 [32]. In Fig. 2(b), one sees that our datasets for the shortest and longest F-actin are close to those for rigid rods and flexible chains, respectively. Data for the ensemble average of the polydisperse F-actin sample fall between these extremes.

The calculated rotational diffusion coefficient of individual F-actin chains is small, $D_r \approx 1.5 \times 10^{-6}\ \mathrm{rad}^2/\mathrm{s}$, meaning that molecular orientations in the rest state do not time average over the experimental time window. Therefore, in the rest state those filaments oriented normal to the focal plane show up as "short chains" with anomalously small length-diameter ratio (<3) in the raw images. This tendency disappears even for our smallest shear rate of 0.001 s^{-1}, at which the Peclet number is $\mathrm{Pe} = \dot{\gamma}_{\min}/D_r \approx 700 \gg 1$. Physically, this means that even at the smallest shear rates at which our measurements were performed, chains are strongly driven to orient in the shear direction.

The data also imply shear-induced stretching, even for these filaments whose mean length was less than their persistence length. To assess the degree of stretching, we compared the end-to-end distance (l) to the actual filament length (L), for all three subpopulations of L. As shown in Fig. 3(a), the probability distribution shifts systematically to larger l/L as shear rate increases. Dissecting this effect according to subpopulations in the polydisperse sample, Fig. 3(b) shows that the subpopulation with largest L displays the strongest dependence, implying that the longest filaments experience the most shear-induced stretching. Moreover, all filaments—even the subpopulation of smallest L—are characterized by distinctly different shear dependence according to whether $\tau_R\dot{\gamma} < 1$ or $\tau_R\dot{\gamma} > 1$, the shear rate dependence being larger in the latter case [Fig. 3(b) specifies the shear rate dependence of each subpopulation in each regime]. On physical grounds, it is reasonable to expect longer filaments to stretch the most, in part because they are most highly entangled, in part because they are most flexible. The present experiments cannot discriminate the relative importance of these influences, both of which tend to produce the same effect.

We now introduce quantification of the tube diameter, as vast theoretical literature [1–5] models the dynamic localization of entangled polymers as diffusion in an effective

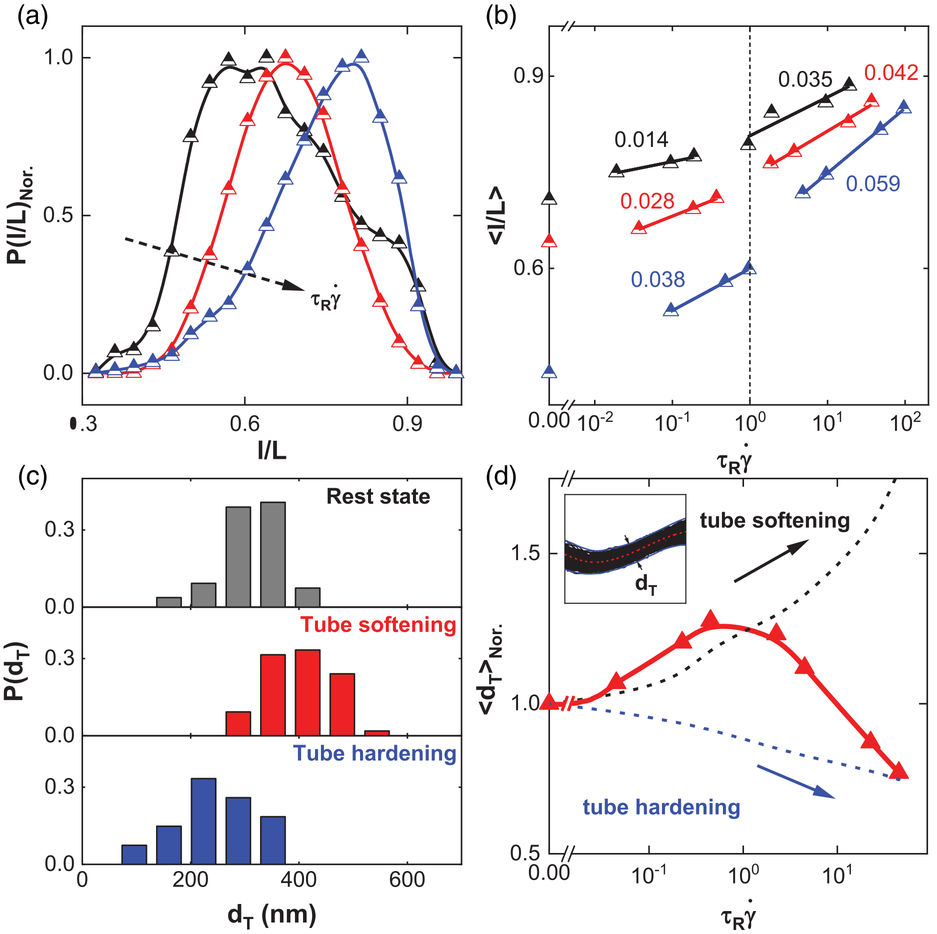

FIG. 3. Tube nonlinearities. (a) Distribution of stretch (l/L), normalized to the peak value, for entangled F-actin filaments at rest (black), at 0.001 s^{-1} (red), and at 1 s^{-1} (blue). (b) Stretch (l/L) plotted against logarithmic shear rate for the subpopulations of shortest, medium-length, and longest filaments (black, red, and blue, respectively). (c) Probability distribution of mean tube size of medium-length filaments in the rest state (gray), at 0.01 s^{-1} (red), and at 1 s^{-1} (blue). (d) Mean tube diameter of medium-length filaments plotted against the logarithmic product of shear rate and Rouse relaxation time, normalized to the mean tube diameter in the rest state. The two dotted lines compare to theoretical predictions [12,14] for "tube softening" and "tube hardening." The inset shows schematically the definition of tube diameter d_T.

tube that represents the collective topological influence of surrounding chains. For F-actin filaments at rest, prior fluorescence-based imaging studies determined the tube diameter by superposing a sufficient number of transient contour lines of the diffusing molecules, determining the mean confining tube diameter $\langle d_T\rangle$ from averaging the width of the bundles along these contours [19,26]. We adapted the same strategy except that it was necessary to first remove directional motion caused by shear flow, which we quantified as the mean velocity of several neighboring F-actin filaments in the same focus plane. Though execution of this strategy demands a dataset of hundreds of well-resolved frames to obtain the tube diameter of even a single molecule, we found it possible to obtain reliable data, at each shear rate, for 50 F-actin filaments whose chain length was 10 ± 1 μm. Rouse chains of this length should have calculated relaxation time $\tau_R \approx 45$ s. These tube diameters $\langle d_T\rangle$ were compared to $\langle d_{T_0}\rangle = 0.32$ μm, the tube diameter we measured in the rest state. It has been predicted from theoretical modeling that though the value in the rest state is dictated by the mesh size, $\xi\,(\mu\mathrm{m}) = 0.3/\sqrt{c\,(\mathrm{mg/ml})} = 0.3$ μm, the value under shear couples to chain alignment and stretching [12–15]; our data confirm this prediction. The probability distributions of tube diameters in the rest state, at modest shear rate, and at high shear rate display major differences plotted in Fig. 3(c).

With increasing shear rate, the ratio $\langle d_T\rangle/\langle d_{T0}\rangle$ increases, reaches a maximum, and undergoes subsequent gentle decline [Fig. 3(d)]. The peak of $\langle d_T\rangle/\langle d_{T0}\rangle$ occurs strikingly close to $\tau_R\dot{\gamma} \approx 1$. Physically, this signifies that when $\tau_R\dot{\gamma} < 1$, shear-induced filament alignment appears to dominate: with increasing alignment, chains can more easily fluctuate normal to their contour, so one observes tube "softening." But when $\tau_R\dot{\gamma} > 1$, chain stiffness increases when hydrodynamic drag forces stretch the filaments, so one observes tube "hardening" [13,14].

Figure 3(d) also shows that these data are qualitatively, though not quantitatively, consistent with the predictions by Schweizer and Sussman regarding the competition between tube softening from affine deformation, $\langle d_T \rangle / \langle d_{T0} \rangle = 1/\sqrt{1 - \langle P_2 \rangle}$ [12], and tube hardening, $\langle d_T \rangle / \langle d_{T0} \rangle = \lambda^{-0.5}$ [14]. Molecular alignment leads to tube dilation, while molecular stretching leads to tube compression, and these effects compete. To the best of our knowledge, there exist no other single-molecule experimental measurements with which to compare.

In addition to the mechanisms discussed above, a third influence has come to be well understood, the end-over-end "tumbling" expected at high shear rate especially for short filaments [29,30]. This is predicted to cause tube entanglement to disappear owing to lessened local chain concentration. This physical situation did not appear to be realized in the current physical system because shear-induced chain scission intervened in the relevant range of high shear rate.

In summary, by using a homebuilt rheo-microscope, we track alignment and stretching during steady-state shear of individual entangled F-actin filaments of different chain lengths. Comparing filament alignment and shear thinning, we observe that the longest F-actin chains in a polydisperse mixture are most flexible, while the shortest F-actin chains are most rigid. With increasing shear rate, we observe dynamical tube nonlinearity, tube softening followed by hardening. Physically, this means that dynamical localization first weakens owing to molecular alignment, then strengthens owing to filament stretching, even for semiflexible biopolymers shorter than their persistence length. This rheo-microscope approach to image single molecules in nonequilibrium mechanical states focuses in on molecular behavior that underlies well-known rheological properties and helps access physical interpretation with improved clarity.

This work is supported by the Institute for Basic Science (Korea), Project No. IBS-R020-D1. Z. Z. and B. C. were supported by the National Natural Science Foundation of China (Grant No. 51825601).

---

[*] These authors contributed equally to this work.

[†] sgranick@gmail.com

[1] P. G. de Gennes, J. Chem. Phys. **55**, 572 (1971).

[2] M. Doi, S. F. Edwards, and S. F. Edwards, *The Theory of Polymer Dynamics* (Oxford University Press, New York, 1988), Vol. 73.

[3] T. McLeish, Adv. Phys. **51**, 1379 (2002).

[4] P. Lang and E. Frey, Nat. Commun. **9**, 1 (2018).

[5] A. Karatrantos, R. J. Composto, K. I. Winey, M. Kröger, and N. Clarke, Polymers **11**, 876 (2019).

[6] C. D. Chapman and R. M. Robertson-Anderson, Phys. Rev. Lett. **113**, 098303 (2014).

[7] T. T. Falzone, S. Blair, and R. M. Robertson-Anderson, Soft Matter **11**, 4418 (2015).

[8] T. T. Falzone and R. M. Robertson-Anderson, ACS Macro Lett. **4**, 1194 (2015).

[9] K.-W. Hsiao, J. Dinic, Y. Ren, V. Sharma, and C. M. Schroeder, Phys. Fluids **29**, 121603 (2017).

[10] D. Mead, R. Larson, and M. Doi, Macromolecules **31**, 7895 (1998).

[11] R. S. Graham, A. E. Likhtman, T. C. McLeish, and S. T. Milner, J. Rheol. **47**, 1171 (2003).

[12] D. M. Sussman and K. S. Schweizer, J. Chem. Phys. **139**, 234904 (2013).

[13] P. de Gennes, MRS Bull. **16**, 20 (1991).

[14] K. S. Schweizer and D. M. Sussman, J. Chem. Phys. **145**, 214903 (2016).

[15] S.-J. Xie and K. S. Schweizer, Soft Matter **14**, 7052 (2018).

[16] S.-Q. Wang, S. Ravindranath, and P. Boukany, Macromolecules **44**, 183 (2011).

[17] See Supplemental Material at http://link.aps.org/supplemental/10.1103/PhysRevLett.129.147801 for more detailed information on materials and polymerization, rheo-microscopy, featuring and tracking individual F-actin filaments, and rheological flow curve.

[18] S.-J. Xie and K. S. Schweizer, Macromolecules **51**, 4185 (2018).

[19] B. Wang, J. Guan, S. M. Anthony, S. C. Bae, K. S. Schweizer, and S. Granick, Phys. Rev. Lett. **104**, 118301 (2010).

[20] K. Zheng, K. Chen, W. Ren, J. Yang, and J. Zhao, Macromolecules **55**, 1647 (2022).

[21] J. Viamontes, P. W. Oakes, and J. X. Tang, Phys. Rev. Lett. **97**, 118103 (2006).

[22] J. He, J. Viamontes, and J. X. Tang, Phys. Rev. Lett. **99**, 068103 (2007).

[23] R. Zhang, N. Kumar, J. L. Ross, M. L. Gardel, and J. J. De Pablo, Proc. Natl. Acad. Sci. U.S.A. **115**, E124 (2018).

[24] M. Dichtl and E. Sackmann, Proc. Natl. Acad. Sci. U.S.A. **99**, 6533 (2002).

[25] B. Tsang, Z. E. Dell, L. Jiang, K. S. Schweizer, and S. Granick, Proc. Natl. Acad. Sci. U.S.A. **114**, 3322 (2017).

[26] J. Käs, H. Strey, and E. Sackmann, Nature (London) **368**, 226 (1994).

[27] M. Abadi, M. F. Serag, and S. Habuchi, Nat. Commun. **9**, 5098 (2018).

[28] P. S. Doyle, B. Ladoux, and J.-L. Viovy, Phys. Rev. Lett. **84**, 4769 (2000).

[29] C. M. Schroeder, R. E. Teixeira, E. S. G. Shaqfeh, and S. Chu, Phys. Rev. Lett. **95**, 018301 (2005).

[30] M. Harasim, B. Wunderlich, O. Peleg, M. Kröger, and A. R. Bausch, Phys. Rev. Lett. **110**, 108302 (2013).

[31] H. Isambert and A. Maggs, Macromolecules **29**, 1036 (1996).

[32] S. Förster, M. Konrad, and P. Lindner, Phys. Rev. Lett. **94**, 017803 (2005).

[33] C. Lang, J. Kohlbrecher, L. Porcar, and M. P. Lettinga, Polymers **8**, 291 (2016).